Appl. Phys. B 76, 191–197 (2003)
DOI: 10.1007/s00340-003-1108-8

Applied Physics B
Lasers and Optics

F. HUNEUS✉
B. SCHÄPERS
T. ACKEMANN
W. LANGE

Optical target and spiral patterns in a single-mirror feedback scheme

Institut für Angewandte Physik, Westfälische Wilhelms-Universität Münster, Corrensstraße 2/4,
48149 Münster, Germany

Received: 31 July 2002/Revised version: 30 October 2002

ABSTRACT Spatio-temporal structures with a regular time dependence are observed in a nonlinear optical system consisting of a sodium-vapour cell and a single feedback mirror. Target and spiral patterns appear spontaneously in the intensity of the transmitted light field as a result of a self-organisation process. In contrast to the results obtained in most other pattern-forming systems, the radial motion of the waves is directed towards the centre. The emergence of oscillatory structures is traced back to a Hopf bifurcation at a finite wave number. The preference for a radial drift motion is due to a nonlinear guiding effect which results from phase gradients created by the inhomogeneous pump profile. The direction of the drift can be reversed by externally applied phase gradients. The system is a striking example of a case in which the radial variation of the pump profile has a decisive influence on pattern formation.

PACS 42.65.Sf; 42.65.Jx; 47.54.+r

1 Introduction

Target and spiral patterns are beautiful manifestations of self-organised spatio-temporal patterns occurring in many systems driven away from thermal equilibrium. Archetypal examples are chemical reactions [1, 2] and the chemotaxis of some biological specimens [3, 4], but similar patterns occur in electrochemistry [5], heterogeneous catalysis [6], Faraday experiments and convection instabilities [7].

Many features of these patterns can be understood in the framework of complex Ginzburg–Landau equations [8, 9]. Hence, a lot of interest was triggered by a paper of Coullet et al. [10] demonstrating that – under suitable conditions – the Maxwell–Bloch equations describing the spatio-temporal dynamics of a laser can be reduced to a Ginzburg–Landau equation, which admits spiral solutions. These spirals were termed optical vortices and represent phase singularities of the optical field. Phase singularities were observed and analysed in a variety of optical systems (see the reviews [11–13]). These spiral patterns are phase spirals and thus are not directly observable with the eye or a camera. Intensity spirals were observed in nonlinear feedback systems in which the rotational symmetry is broken due to a rotation of the feedback loop [14]. More recently, intensity spirals were also predicted to occur in a rotationally symmetric system, an internally pumped optical parametric oscillator [15].

In this paper we report the experimental observation of target and spiral patterns in the intensity distribution transmitted by a single-mirror feedback scheme. The unstructured system has rotational symmetry. In contrast to the results obtained in other systems (see [16] for a recent exception), the motion of the rings of a target pattern (or the arms of a spiral) is not directed outwards, but inwards, i.e. towards the core. It is shown that the drift direction is determined by nonlinear phase gradients, i.e. by phase gradients induced by the intensity profile of the pump beam. The drift direction can be reversed by introducing suitable phase distributions externally.

In the case of a plane-wave input the emergence of periodic structures like rhombs or hexagons is expected under the conditions of the experiment [17]. These structures should not be stationary, but display a periodic time dependence due to the presence of a Hopf instability. Thus the observations provide a striking example of a situation in which the pattern-forming process is totally changed by a spatial dependence of the control parameter, which is the input intensity in this case.

The system is analysed by means of a linear stability analysis and it is confirmed by numeric solutions of the model equations describing the system that indeed nonlinear guiding and/or the spatial dependence of saturated absorption in the inhomogeneous input beam give rise to the behaviour observed in the experiment.

2 Experimental setup

The system under consideration is a realisation of the single-mirror feedback scheme analysed in [18]. In the present experiment sodium vapour in a buffer gas and held under carefully chosen operating conditions is utilised as the nonlinear medium. The experimental setup consists of three main parts: the nonlinear medium, the optical system providing the light field in the medium and the analysis optics. Parts of the experimental scheme are shown in Fig. 1.

A glass cell contains sodium vapour at a temperature T_{cell} of about 340 celsius in a nitrogen buffer-gas atmosphere (pres-

---

✉ Fax: +49-251/83-33513, E-mail: huneus@uni-muenster.de

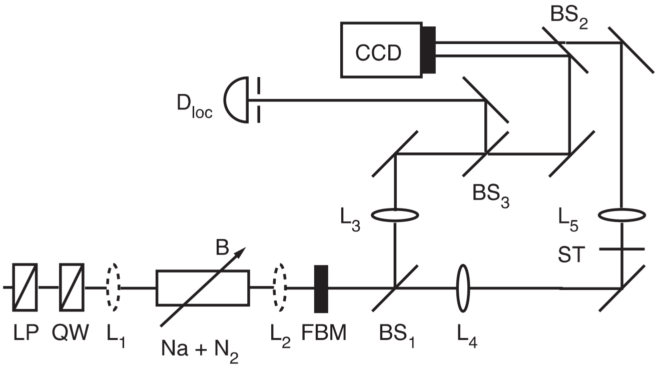

FIGURE 1 Schematic experimental setup. LP: linear polariser, QW: quarter-wave plate, L_1, L_2: lenses (optionally inserted), FBM: feedback mirror, B: magnetic field, L_3, L_4, L_5: lenses, BS_1, BS_2, BS_3: beam splitters, ST: stop

sure p_{N_2}, typically 300–320 hPa). The cell is surrounded by three orthogonal pairs of Helmholtz coils, which can compensate the Earth's magnetic field or create an oblique dc magnetic field. The latter changes the optical properties of the sodium vapour.

A frequency-stabilised cw dye laser serves as light source. It is typically tuned to a frequency about 10 GHz above the sodium D_1 resonance. The laser beam is spatially filtered by means of a single-mode optical fibre and circularly polarised by a combination of a linear polariser and a quarter-wave plate. The intensity of the laser light can be varied with the help of an electro-optical modulator. A telescope is used to control the beam parameters of the laser and allows us to place the beam waist into the sodium-vapour cell. The beam radius at the $1/e^2$ point of intensity is ~ 1.5 mm, corresponding to a Rayleigh length of ~ 12 m.

The feedback mirror is located at a distance d behind the vapour and reflects more than 90 percent of the power back into the nonlinear medium. In some of the experiments reported in the following the setup is modified by inserting an additional lens, either located directly in front of the cell (L_1) or between the nonlinear medium and the mirror (L_2).

The small amount of light transmitted by the feedback mirror is used to analyse the emerging structures. For this purpose, the optical field in the plane $2d$ behind the cell, which corresponds to the reentrant field distribution, is imaged on one-half of the chip of a CCD camera. On the other half of the CCD chip the far-field distribution produced by a lens in a $2f$ scheme is imaged, with the central region, including the zero wave number, being blocked by a stop. The CCD camera is equipped with a microchannel plate as a fast shutter (integration time typically 1 μs) and provides 8-bit grey-scaled images of 768 × 576 pixels size. By this setup synchronised and time-resolved images of the near and the far field are obtained. In another arm a photo-diode located behind a pinhole is placed in the plane of the near-field image. Its output signal represents a local intensity. It allows us to distinguish between stationary and dynamic structures and provides a trigger for the 'video-sampling method' [19]. This technique generalises the operating principle of a sampling scope to time-resolved image analysis of fast repetitive processes by means of basically slow image-acquisition equipment. It relies on scanning the delay between a suitable trigger signal and a fast shutter, which is formed by the microchannel plate in this case.

3 Experimental observation of spirals and target patterns

Figure 2a to h show typical snapshots of structures that can be observed in the transverse intensity profile of the laser beam if the input power is increased above a certain threshold. Both target patterns and spirals occur, the latter having a varying number of arms. Each of the spiral arms has an Archimedian shape. Spirals can possess opposite chirality, see e.g. Fig. 2b and c. The structures can be observed for periods of time between milliseconds and some minutes. For constant parameters, the system exhibits spontaneous switching between target patterns and spirals as well as between spirals with different chirality or a different number of arms.

Simultaneously with the appearance of the structures the signal of the photo-diode becomes oscillatory and thus indicates a periodic time dependence of the local intensity. Using this signal as a trigger for the video-sampling system reveals that the target patterns and spirals are not stationary but dynamic structures. Such video-sampling sequences show that the rings of the target patterns move towards the centre of the beam and disappear there, while new rings are constantly born at the boundary. For a spiral, in Fig. 3 intensity profiles obtained from cuts through the images of a video-sampling sequence are arranged to illustrate the radial motion in a space–time diagram. Obviously, radial motion is directed inwardly. This results in an up-winding rotation of the structure, which is in contrast to spirals in many other systems [1, 2, 4, 8, 9].

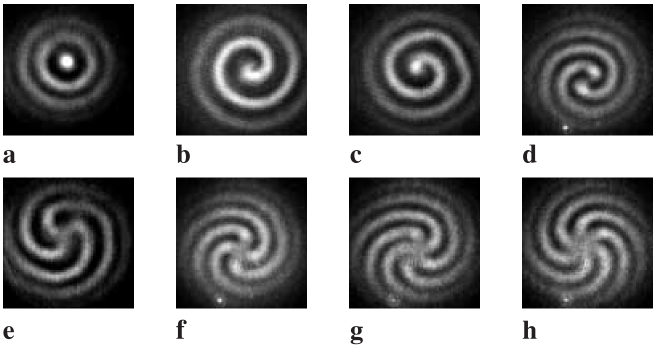

FIGURE 2 Snapshots of structures spontaneously emerging in the transverse intensity profile of the laser beam for typical experimental parameters: **a** target pattern, **b**, **c** one-armed spirals with opposite chirality, **d**–**h** two- to six-armed spirals. The images are displayed in a linear grey-level coding with 'black' denoting low intensity

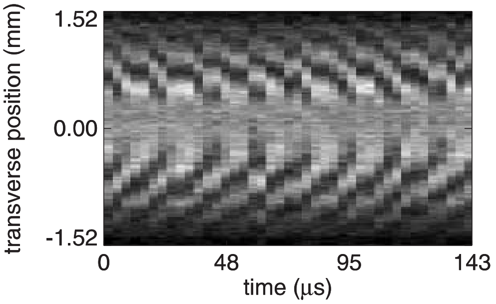

FIGURE 3 Space–time plot illustrating radial motion in the observed structures. Parameters: $d = 65$ mm, $\Delta = 10.3$ GHz, $B_\perp = 4.2\,\mu$T, $B_z = 14.4\,\mu$T, $T_{cell} = 346\,°$C, $p_{N_2} = 314$ hPa, $P_{in} = 135$ mW

The time series obtained from the signal of the photodiode shows a rather regular harmonic oscillation so that a characteristic frequency can be assigned to each set of parameters. The frequency has a strong dependence on the experimental parameters (see below) and ranges from tens of kHz up to approximately 500 kHz. It is constant over the cross section of the beam. The existence of a characteristic frequency is used as a delimiting criterion for the domain of oscillatory structures in parameter space. Since it turns out that the components of the magnetic field transverse and longitudinal to the direction of light propagation have a strong influence on the patterns, these two components are used as coordinates in Fig. 4 where the domain of time-dependent structures is depicted. The observed scenario possesses an approximative reflection symmetry with respect to zero of the transverse magnetic field. For both signs of the transverse magnetic field, two regions are found where structures with an oscillatory time dependence of the local intensity exist. With increasing transverse component the edges of these domains are shifted to higher absolute values of the longitudinal magnetic field. The corresponding characteristic frequencies are depicted in Fig. 5. They are strongly dependent on the transverse and longitudinal field components and scale approximately linearly with both of them.

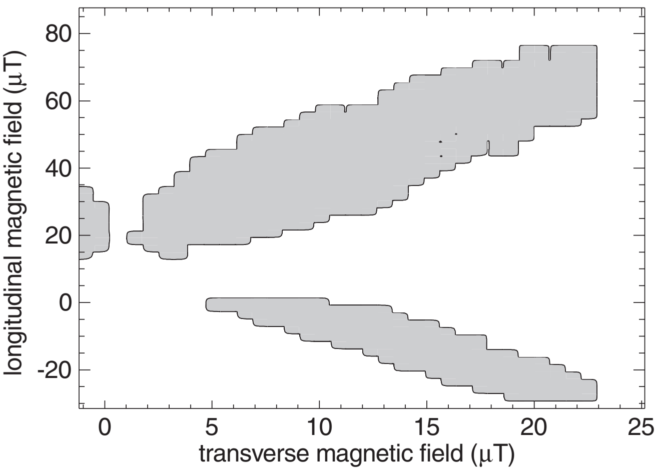

FIGURE 4 Domain of structures with oscillatory time dependence of the local intensity in dependence on the components of the magnetic field. Parameters: $d = 65$ mm, $\Delta = 11.5$ GHz, $T_{\text{cell}} = 339$ °C, $p_{\text{N}_2} = 302$ hPa, $P_{\text{in}} = 130$ mW

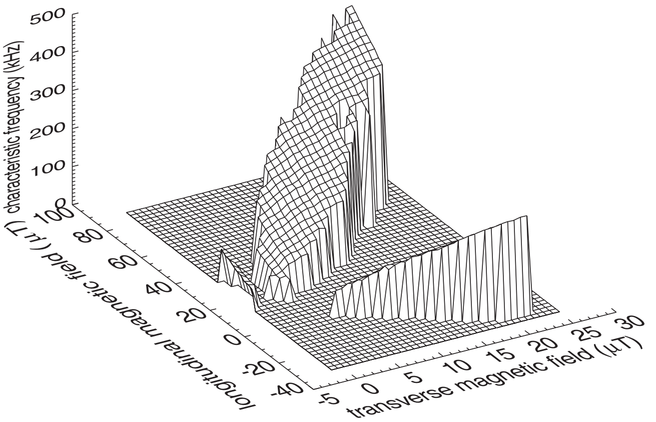

FIGURE 5 Characteristic frequency as a function of the components of the magnetic field. Parameters: $d = 65$ mm, $\Delta = 11.5$ GHz, $T_{\text{cell}} = 339$ °C, $p_{\text{N}_2} = 302$ hPa, $P_{\text{in}} = 130$ mW

4 Theoretical analysis

4.1 *Theoretical model*

In the analysis of the experiments a model is used which has been proven to be adequate in numerous similar experiments [20–23]; details can be found in the literature [20, 23, 24]. Under the conditions of the experiment the model describes the atoms by means of a homogeneously broadened $J = \frac{1}{2} \leftrightarrow J' = \frac{1}{2}$ transition. Optical pumping by circularly polarised light creates a population difference between the Zeeman substates of the ground state, i.e. an 'orientation' of the sample. This results in a change of the optical properties of the sample, i.e. it gives rise to a nonlinearity.

The existence of the orientation implies the existence of a nonvanishing expectation value of a macroscopic magnetic moment in the sample. The interaction of this magnetic moment with the oblique magnetic field is crucial in the experiment. In a formal description it is convenient to introduce the Bloch vector $\boldsymbol{m} = (u, v, w)$, whose components are proportional to the expectation values of the Cartesian components of the magnetic moment. The temporal evolution of $\boldsymbol{m}$ is described by the partial differential equation [20, 23]:

$$\begin{aligned}\frac{\mathrm{d}}{\mathrm{d}t}\boldsymbol{m} = &-\gamma\boldsymbol{m} + D\Delta_\perp\boldsymbol{m} - P(w,\ \Delta_\perp w)\boldsymbol{m} \\ &-\boldsymbol{m}\times\boldsymbol{\Omega} + \hat{\boldsymbol{e}}_z P(w,\ \Delta_\perp w)\,. \end{aligned} \tag{1}$$

Here γ is a constant describing the relaxation of $\boldsymbol{m}$. Its value is approximately 1 s^{-1}. D is the diffusion constant and $\Delta_\perp$ is the transverse part of the Laplacian. P is the pump rate induced by the light field (and it is dependent on both w and $\Delta_\perp w$) and $\boldsymbol{\Omega}$ is a torque vector defined by $\boldsymbol{\Omega} = (\Omega_x, 0, \Omega_z - \bar{\Delta}P)$. Here the direction of the laser beam defines the z axis and the x axis is chosen in the direction of the transverse component of the magnetic field. Ω_x and Ω_z are the Larmor frequencies produced by the x and z components of the magnetic field, respectively. The term $-\bar{\Delta}P$ in the z component of $\boldsymbol{\Omega}$ is due to a light-induced level shift ('light shift') occurring in a slightly off-resonant monochromatic light field [25]. $\bar{\Delta}$ is the suitably normalised detuning of the laser with respect to the resonance line.

While the first term of the differential equation describes the relaxation of $\boldsymbol{m}$, the second term describes the influence of thermal diffusion. The third term describes saturation. The vector product describes the interaction of $\boldsymbol{m}$ with a generalised magnetic field, i.e. the Larmor precession. The production of orientation by Zeeman pumping is described by the last term of the equation. It can be seen that only the component w of $\boldsymbol{m}$ is driven directly by Zeeman pumping.

It turns out that the nonlinear complex susceptibility is related to the linear one, χ_{lin}, by:

$$\chi = \chi_{\text{lin}}(1 - w)\,, \tag{2}$$

i.e. the nonlinearity is determined only by the (intensity-dependent) component w of the Bloch vector.

The pump rate P is proportional to the local intensity, which is in an approximation described by adding the intensities of the forward- and the backward-travelling beams.

In the calculation of the intensities it is taken into account that a possible spatial dependence of w in the sample imposes a spatial phase and amplitude modulation on the transmitted beam. Its evolution in the propagation from the cell to the feedback mirror and back is calculated by integrating the paraxial wave equation by means of Fourier methods.

4.2 *Linear stability analysis*

In a linear stability analysis (LSA) the stability of the homogeneous stationary solution of $\boldsymbol{m}$ against spatially inhomogeneous perturbations is examined, which are assumed to be Fourier modes with a transverse wave number q. If the resulting intensity distribution in the reflected beam enhances the initial perturbation, then an instability develops. Mathematically the LSA describes the evolution of small deviations of $\boldsymbol{m}$ from the homogeneous solution by a linearised differential equation which is homogeneous and thus leads to an eigenvalue problem. In Fig. 6 regions of instability are displayed in dependence on the pump rate and the transverse wave number. Regions where one eigenvalue is positive are grey-shaded, whereas those in which a pair of complex conjugate eigenvalues has a positive real part are hatched. In the former case a stationary spatial modulation will grow (static instability), while there is a so-called Hopf instability in the latter case, i.e. here the homogeneous solution is unstable against perturbations oscillating in space and time. In the beginning of the evolution the frequency of the temporal oscillation is given by the imaginary part of the eigenvalue. Because of saturation of the optical medium the curves of marginal stability, defined by vanishing of the real parts of the corresponding eigenvalues, are closed for all instabilities.

At large pump rates, which are not reached in the experiments considered in this work, there is a static instability in the wave-number range from zero to $\sim 20\,\mathrm{rad\,mm^{-1}}$. The case of $q = 0$ being unstable corresponds to whole-beam switching [22]. It is typical for pattern formation in diffractive systems [18, 26] that there is also a corresponding instability region at higher q ($q > 30\,\mathrm{rad\,mm^{-1}}$) in the displayed parameter region. At lower pump rates another static instability occurs between wave numbers of ~ 22 to $29\,\mathrm{rad\,mm^{-1}}$. Moreover a Hopf instability occurs for values of q around $12.7\,\mathrm{rad\,mm^{-1}}$. The range of unstable wave vectors does not extend to $q = 0\,\mathrm{rad\,mm^{-1}}$ and therefore whole-beam oscillations are not expected. It is tempting to assume that the time-dependent structures observed in the experiment are somehow related to the Hopf instability. This will be confirmed in the following.

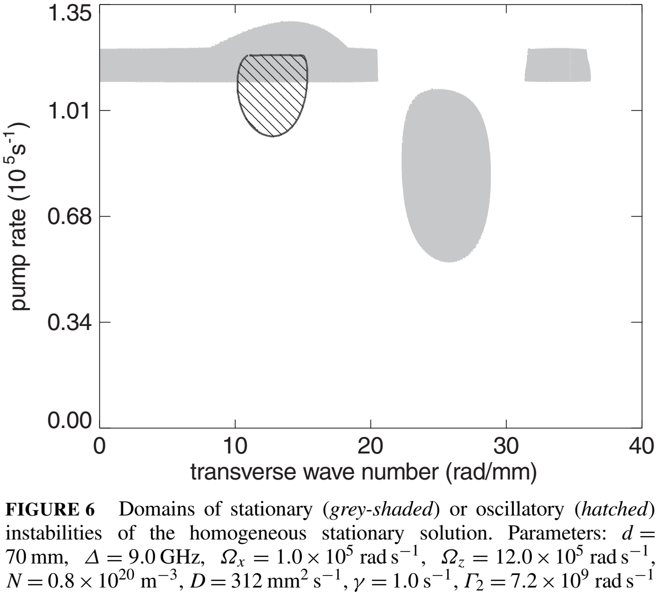

FIGURE 6 Domains of stationary (*grey-shaded*) or oscillatory (*hatched*) instabilities of the homogeneous stationary solution. Parameters: $d = 70\,\mathrm{mm}$, $\Delta = 9.0\,\mathrm{GHz}$, $\Omega_x = 1.0 \times 10^5\,\mathrm{rad\,s^{-1}}$, $\Omega_z = 12.0 \times 10^5\,\mathrm{rad\,s^{-1}}$, $N = 0.8 \times 10^{20}\,\mathrm{m^{-3}}$, $D = 312\,\mathrm{mm^2\,s^{-1}}$, $\gamma = 1.0\,\mathrm{s^{-1}}$, $\Gamma_2 = 7.2 \times 10^9\,\mathrm{rad\,s^{-1}}$

4.3 *Numerical simulations*

Numerical simulations of the model equations are carried out using a hopscotch algorithm to model the time evolution. For the treatment of propagation the transmitted light field is Fourier transformed. Then the propagation operator is applied in the Fourier space. An inverse transformation yields the reflected field if one takes into account the reflectivity of the feedback mirror. Simulations include spatially and temporally low-pass filtered noise and are realised on grids with 128×128 or 256×256 points. The simulations are performed with plane-wave input and periodic boundary conditions as well as with a Gaussian-shaped pump profile and Dirichlet boundary condition $\boldsymbol{m} = 0$ on a circular edge representing the wall of the cell.

In simulations with a Gaussian-shaped input beam target patterns and spirals are found which are very similar to the experimental structures (Fig. 7). They show multi-stability and have an oscillatory time dependence of the local intensity as in the experiment. The direction of radial motion is apparent in the space–time plot in Fig. 8. It is directed towards the centre of the beam and is thus in agreement with the unexpected experimental result. Transitions from target patterns to spirals occur spontaneously in the calculations, but spontaneous switching from spirals to target patterns or between spirals of different chirality has not been observed yet in the simulations, while they occur in the experiment. This discrepancy is assumed to be due to inadequate modelling of the noise in the calculations.

In simulations with plane-wave input, structures with an oscillatory dependence of the local intensity have been found before [17] for similar model parameters. Instead of target patterns and spirals these structures were so-called ‘winking

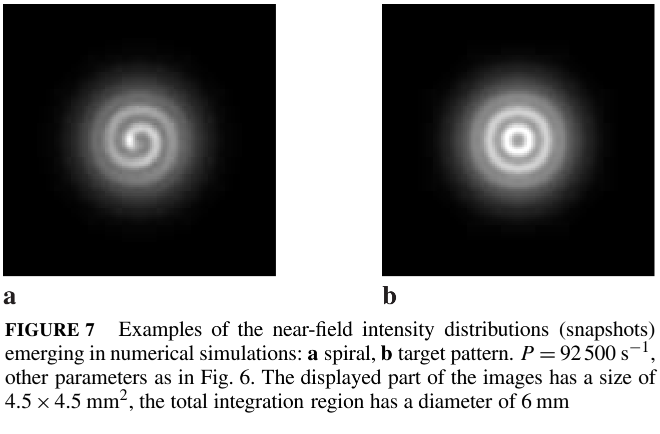

FIGURE 7 Examples of the near-field intensity distributions (snapshots) emerging in numerical simulations: **a** spiral, **b** target pattern. $P = 92\,500\,\mathrm{s^{-1}}$, other parameters as in Fig. 6. The displayed part of the images has a size of $4.5 \times 4.5\,\mathrm{mm^2}$, the total integration region has a diameter of 6 mm

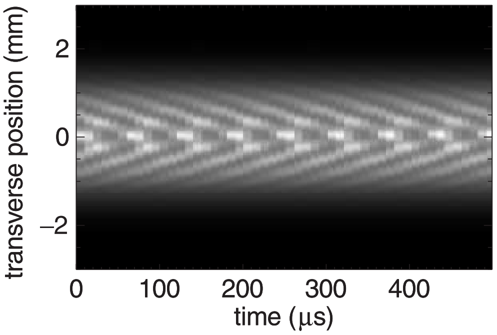

FIGURE 8 Space–time plot illustrating radial motion in numerical simulations. Parameters as in Fig. 7

hexagons', i.e. periodically varying patterns with hexagonal symmetry which emerge as a result of interaction between the Hopf instability and the static instability. So, there is a pronounced difference between the results of the simulations using a Gaussian beam, which agree well with the experimental ones, and numerical plane-wave results. We will analyse possible reasons in the following.

5 Origin of radial motion and selection of its direction

5.1 *Theoretical results*

In the calculations, target patterns and spirals are obtained in a parameter range where the (nonlinear) index of refraction decreases with increasing values of the pump rate. That means that the inner parts of a Gaussian-shaped input beam, where the pump rate is large, experience a lower index of refraction than the outer ones, so that the phase of the transmitted light field is subjected to a radial variation (Fig. 9). The displayed plot is a result of a numerical simulation in which pattern formation is suppressed by means of blocking the corresponding spatial frequencies in the feedback beam, i.e. by means of appropriate Fourier filtering. It can be seen that the inner part of the beam, where pattern formation takes place without Fourier filtering, displays a phase distribution more or less similar to that caused by a defocusing lens. In order to estimate the power of the corresponding lens a parabola (dashed) is fitted to this part of the beam. This fit yields an effective focal length of approximately −2.2 m.

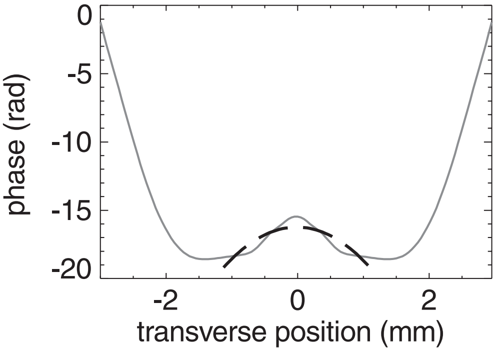

FIGURE 9 Phase of transmitted field in numerical simulations with a Fourier filter suppressing structuring. The *dashed line* is the parabola fitting best to the phase profile in the part of the beam exhibiting pattern formation without a filter. Parameters as in Fig. 7

It is apparent from Fig. 9 that there is an interval of positions on both sides of the origin in which the phase decreases monotonically with increasing distance to the centre. Let us assume for a moment that there is a linear variation of the phase. This may give some insight with respect to possible consequences of phase gradients.

It is a well-known fact that a constant phase gradient induces a drift motion in an infinitely extended system [27, 28]. For a formal treatment of the present case, the linear stability analysis of the homogeneous state has to be extended in order to take into account the shift of the feedback field caused by the phase gradient. It turns out that a spatial structure which is stationary without the additional gradient will drift antiparallel to the gradient. The effect of a gradient on the Hopf modes is a breaking of the degeneracy between the two complex conjugate solutions corresponding to the pair of complex conjugate eigenvalues which exist for zero phase gradient. The threshold for one of the modes increases, the one for the other mode decreases. The latter – i.e. the favoured one – is the one for which the phase velocity is directed parallel to the phase gradient.

The change of threshold due to the phase gradient can be quite pronounced. This becomes apparent by a comparison between Fig. 10a and b. Both figures display the regions in

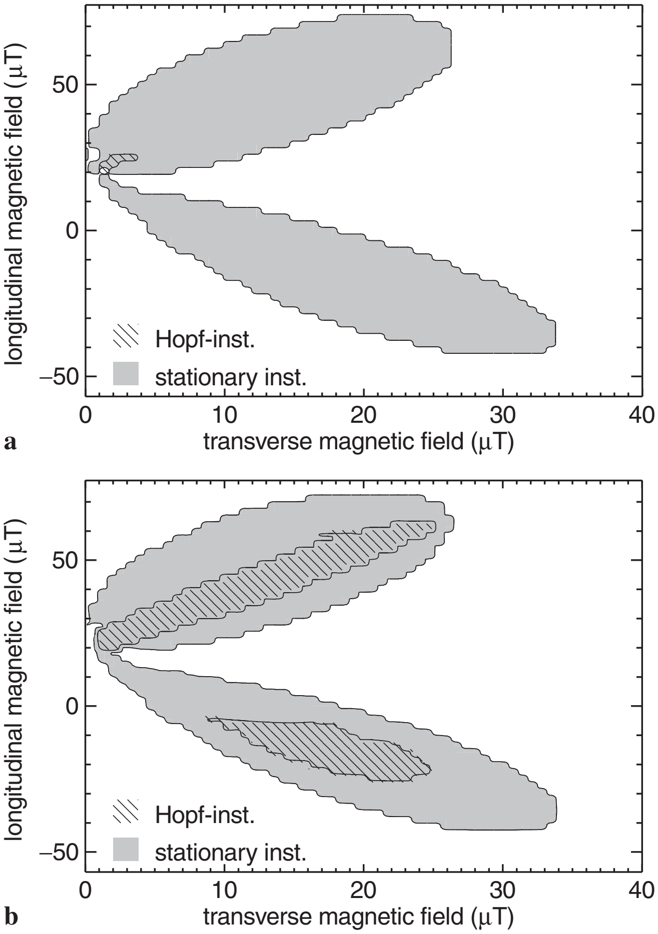

FIGURE 10 Regions of stationary (*grey-shaded*) and Hopf instabilities (*hatched*) in the LSA in dependence on the magnetic field. **a** Isotropic case, **b** with additional phase gradient $\delta\phi/\delta x = 0.2\ \text{rad/mm}$; other parameters as in Fig. 7

which the homogeneous state is linearly unstable in a parameter space spanned by the transverse and longitudinal components of the magnetic field. Again, regions belonging to stationary instabilities are grey-shaded. In Fig. 10a, there is no additional phase gradient and the domain of the Hopf instability (hatched) is very small. The scenario changes if a weak phase gradient is introduced (Fig. 10b). Now the Hopf modes are unstable within two regions that have a similar shape as the domains of oscillatory structures observed in the experiment. The corresponding Hopf frequencies are also in a range that is similar to that of the characteristic frequencies observed in the experiment (some tens of kHz up to 500 kHz).

It can be assumed that similar results would be obtained for a nonlinear, but monotonic phase variation. If we assume that the result can even be transferred to a situation of cylindrical symmetry, then we have to expect travelling waves directed to the beam centre, since this is the direction of the phase gradient. This matches nicely the experimental and numerical results. The argument, however, is hand-waving only, of course. For this reason additional numerical and even experimental studies were performed.

If the radial phase distribution introduced by the Gaussian beam is at the origin of the inward-moving structures, then it should be possible to find spirals and target patterns also in simulations with an input pump field of homogeneous intensity, if only an additional phase distribution with sufficiently steep gradients is added to model the interplay of the Gaussian beam and the nonlinear characteristic of the optical medium. In order to avoid discontinuities at the edge of the numerical grid the incorporated additional phase distribution has a two-dimensional Gaussian shape. The simulations confirm the expectation: with ‘focusing’ as well as with ‘defocusing’ phase distributions target patterns and spirals are obtained. While they show an inward motion in the latter case, as in the experiment and in the simulations with a Gaussian beam, they move outwards in the former case. Thus it can be conjectured that a curvature of the phase front causes a transition from oscillating hexagonal structures to moving target patterns and spirals and that the direction of motion is selected by the sign of the curvature of the additional phase distribution.

As a consequence of these simulations the question arises of whether the direction of radial motion can also be manipulated for a Gaussian input beam. Figure 11 pictures the results of numerical simulations with a Gaussian-shaped pump profile and an additional focusing phase distribution, which is normalised so that an expansion up to second order is equivalent to the phase distribution caused by a parabolic lens. By this normalisation an effective focal length can be defined. For a weak, negligible focusing the same structures develop as for a simulation without additional phase: target patterns or spirals moving inwardly (Fig. 11a). Increasing the strength of the additional phase distribution, i.e. shortening the effective focal length, results in completely different structures. An extended nearly hexagonal pattern arises if the induced lens effect ($f = -2.2$ m, see above) is – or at least is nearly – compensated by the additional phase distribution as shown in Fig. 11b for an additional focal length of $f = 2.2$ m. In contrast to the other structures described here, this pattern has no time dependence. Moreover, the length scale matches that of the static instability quite well. Another qualitative change of the emerging structure can be observed for an even shorter focal length. In Fig. 11c the result of numerical simulations incorporating an additional phase distribution with an effective focal length of 800 mm is shown. Again, target patterns and spirals with the length scale of the Hopf instability are generated. In this computation the lens effect induced by the Gaussian beam is overcompensated by the focusing phase distribution so that the phase fronts of the field transmitted by the optical medium have the opposite curvature. Hence, motion in the structures is pointing in the opposite direction, i.e. outwardly.

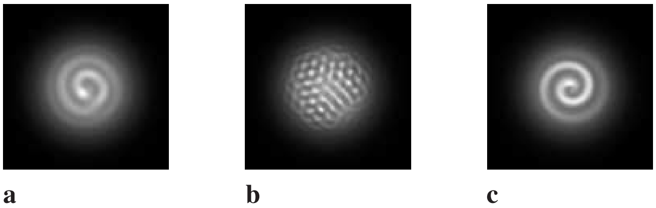

FIGURE 11 Snapshots of near-field intensity distributions obtained from numerical simulations with a Gaussian input beam and an additional focusing phase distribution of focal length **a** 20 000 mm, **b** 2200 mm, **c** 800 mm. Parameters as in Fig. 7

5.2 *Experimental results*

In order to verify the results of the preceding section in the experiment, the lensing effect of the optical medium is determined by measuring the beam radius in dependence on the longitudinal coordinate for the hot and the cold sodium cell. The experiment with the nonlinear medium is done slightly below the threshold of pattern formation. From a fit of beam parameters to the experimental data an effective focal length of approximately -1.6 m is computed for the induced lensing effect. (The difference from the effective focal length calculated for the numerics is not surprising because a different set of parameters is used.)

In the following, experiments are reported in which the induced lensing effect of the optical medium is approximately compensated and overcompensated, respectively, by additional lenses L_1 and L_2 (see Sect. 2). To compensate the induced lensing effect, lens L_1, which has a focal length of 2 m, is placed about 100 mm in front of the cell so that curved phase fronts entering the medium are obtained, whereas the beam radius is nearly unaffected. In Fig. 12 it can be seen that

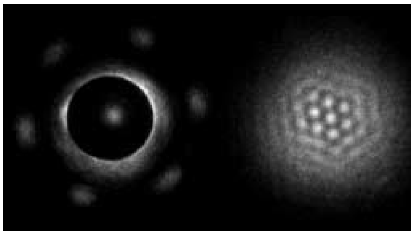

FIGURE 12 Hexagonal pattern with a small length scale due to compensation of the induced lensing effect by an additional lens. *Left part*: far field, *right part*: near field. The structures in the centre of the far-field intensity distribution result from parasitic light passing the blocking spot. Parameters: $d = 65$ mm, $\Delta = 13.5$ GHz, $B_\perp = 7.7\,\mu$T, $B_z = 32.9\,\mu$T, $T_{\text{cell}} = 344.1$ °C, $p_{N_2} = 312$ hPa, $P_{\text{in}} = 192$ mW

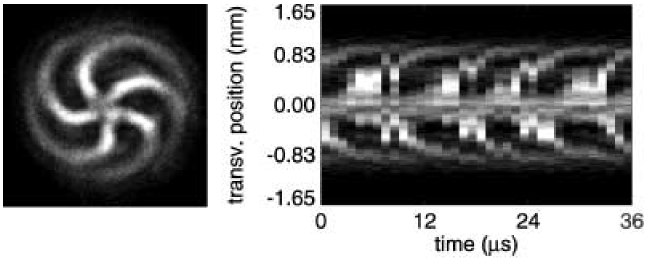

FIGURE 13 Spiral with outwardly directed radial motion due to overcompensation of the induced lensing effect by an additional lens. *Left part*: snapshot of near field, *right part*: space–time diagram. Parameters: $d = 65\,\mathrm{mm}$, $\Delta = 11.3\,\mathrm{GHz}$, $B_\perp = 9.5\,\mu\mathrm{T}$, $B_z = 27.4\,\mu\mathrm{T}$, $T_\mathrm{cell} = 344.5\,°\mathrm{C}$, $p_{\mathrm{N}_2} = 309\,\mathrm{hPa}$, $P_\mathrm{in} = 180\,\mathrm{mW}$

an extended hexagonal pattern is developed. Its length scale ($q = 27.0\,\mathrm{rad\,mm^{-1}}$) is much smaller than that of the Hopf instability but fits that of the static instability quite well.

A lens strong enough to overcompensate the induced lensing effect would change the radius of the beam entering the nonlinear medium considerably. For that reason, a different setup is used in which a lens L_2 ($f = 1000\,\mathrm{mm}$) is placed between the sodium-vapour cell and the feedback mirror. Thus, the radius of the reentrant field is nearly unchanged, but the phase surfaces of the light field, which has passed the lens twice, have a reversed curvature. The emerging structure is shown on the left-hand side of Fig. 13. It is a spiral which is dominated by the length scale of the Hopf instability, as without the lens. Now, however, the radial motion is directed in the outward direction (see the space–time plot on the right of Fig. 13).

6 Conclusion

In this paper target and spiral patterns emerging spontaneously in a single-mirror feedback scheme were analysed from an experimental and a theoretical point of view. The experimental observations are in good agreement with simulations based on a microscopic model, if the appropriate boundary conditions and the spatial variation of the pump profile are taken into account. The appearance of oscillating structures is related to a Hopf bifurcation at a finite wave number of the homogeneous state. However, the actual realisation depends strongly on the boundary conditions and pump profiles present in the experiment. It was shown that the preference for a radial drift motion is due to nonlinear guiding effects which result from phase gradients created by the inhomogeneous pump profile. The direction of the drift is determined by the sign of the curvature of the phase front imposed by the nonlinear interaction with the medium. In the observations reported here it is opposite to the drift direction of the waves in spiral and target patterns known from most other systems.

The system under investigation is a striking example of a case in which the radial variation of the pump profile has a decisive influence on pattern formation. However, on a quantitative level an influence on pattern formation can be expected in many optical systems, since a radial variation of the power is difficult to avoid in systems with an all-optical nonlinearity. For example, the position of localised, soliton-like states within the background beam profile, which exist in nearby parameter ranges in the system under study [23], are also affected by induced phase and amplitude gradients [29]. The results reported here complement predictions of possible effects of the beam profile on the dynamics of nonlinear optical systems (see e.g. [30, 31]).

Future work needs to address the mechanisms of selection between the different kinds of patterns observed experimentally (targets and spirals, spirals with different chirality and spirals with a different number of arms) as well as possible connections between the targets and spirals discussed here and the ones found in other pattern-forming systems.

ACKNOWLEDGEMENTS Financial support of the Deutsche Forschungsgemeinschaft is gratefully acknowledged.

REFERENCES

1 A.T. Winfree: Science **175**, 634 (1972)
2 J. Ross, S.C. Müller, C. Vidal: Science **240**, 460 (1988)
3 G. Gerisch: Naturwissenschaften **58**, 430 (1971)
4 O. Steinbock, H. Hashimoto, S.C. Müller: Physica D **49**, 233 (1991)
5 K. Agladze, O. Steinbock: J. Phys. Chem. **104**, 9816 (2000)
6 S. Jakubith, H.-H. Rotermund, W. Engel, A. von Oertzen, G. Ertl: Phys. Rev. Lett. **65**, 3013 (1990)
7 M. Assenheimer, V. Steinberg: Nature **367**, 345 (1994)
8 Y. Kuramato: *Chemical Oscillations, Waves and Turbulence* (Springer Ser. Synerg. **19**) (Springer, Berlin 1984)
9 L. Kramer, F. Hynne, P.G. Sørenson, D. Walgraef: Chaos **4**, 443 (1994)
10 P. Coullet, L. Gil, F. Rocca: Opt. Commun. **73**, 403 (1989)
11 L.A. Lugiato, M. Brambilla, A. Gatti: Adv. At., Mol., Opt. Phys. **40**, 229 (1999)
12 F.T. Arecchi, S. Boccaletti, P.L. Ramazza: Phys. Rep. **318**, 1 (1999)
13 C.O. Weiss, M. Vaupel, K. Staliunas, G. Slekys, V.B. Taranenko: Appl. Phys. B **68**, 151 (1999)
14 S.A. Akhmanov, M.A. Vorontsov, V.Y. Ivanov: Sov. Phys. JETP Lett. **47**, 707 (1988)
15 P. Lodahl, M. Bache, M. Safmann: Phys. Rev. Lett. **85**, 4506 (2000)
16 V.K. Vanag, I.E. Epstein: Science **294**, 835 (2001)
17 Y.A. Logvin, T. Ackemann: Phys. Rev. E **58**, 1654 (1998)
18 G. D'Alessandro, W.J. Firth: Phys. Rev. Lett. **66**, 2597 (1991)
19 M. Möller, H.J. Bruns: Rev. Sci. Instrum. **66**, 4535 (1995)
20 F. Mitschke, R. Deserno, W. Lange, J. Mlynek: Phys. Rev. A **33**, 3219 (1986)
21 T. Ackemann, Y. Logvin, A. Heuer, W. Lange: Phys. Rev. Lett. **75**, 3450 (1995)
22 T. Ackemann, A. Heuer, Y.A. Logvin, W. Lange: Phys. Rev. A **56**, 2321 (1997)
23 B. Schäpers, T. Ackemann, W. Lange: J. Opt. Soc. Am. B **19**, 707 (2002)
24 M. Möller, W. Lange: Phys. Rev. A **49**, 4161 (1994)
25 C. Cohen-Tannoudji: Ann. Phys. (NY) **7**, 423 (1962)
26 T. Ackemann, W. Lange: Appl. Phys. B **72**, 21 (2001)
27 M. Haelterman, G. Vitrant: J. Opt. Soc. Am. B **9**, 1563 (1992)
28 G. Grynberg: Opt. Commun. **109**, 483 (1994)
29 B. Schäpers, T. Ackemann, W. Lange: IEEE J. Quantum Electron. **39**, scheduled for February 2003
30 S. Coen, M. Tlidi, P. Emplit, M. Haelterman: Phys. Rev. Lett. **83**, 2328 (1999)
31 E. Louvergneaux: Phys. Rev. Lett. **87**, 244 501 (2001)